


Nanometer-Scale-Resolution Multichannel Separation of Spherical Particles in a Rocking Ratchet with Increasing Barrier Heights

Philippe Nicollier^{✉,†}, Christian Schwemmer^{✉,†}, Francesca Ruggeri[✉], Daniel Widmer, Xiaoyu Ma, and Armin W. Knoll^{✉*}

IBM Research—Zurich, Säumerstrasse 4, Rüschlikon 8803, Switzerland

 (Received 24 March 2020; revised 10 November 2020; accepted 25 January 2021; published 2 March 2021)

We present a nanoparticle size-separation device based on a nanofluidic rocking Brownian motor. It features a ratchet-shaped electrostatic particle potential with increasing barrier heights along the particle transport direction. The sharp drop of the particle current with barrier height is exploited to separate a particle suspension into multiple subpopulations. By solving the Fokker-Planck equation, we show that the physics of the separation mechanism is governed by the energy landscape under forward tilt of the ratchet. For a given device geometry and sorting duration, the applied force is thus the only tunable parameter to increase the separation resolution. For the experimental conditions of 3.5 V applied voltage and 20 s sorting, we predict a separation resolution of approximately 2 nm, supported by experimental data for separating spherical gold particles of nominal diameters of 80 and 100 nm.

DOI: [10.1103/PhysRevApplied.15.034006](https://doi.org/10.1103/PhysRevApplied.15.034006)

I. INTRODUCTION

Separation of nanoparticles and molecules is a highly relevant technical task [1], for which the resolution is typically limited by diffusion. Therefore, high driving fields are required to enhance the resolution. For example, in capillary electrophoresis [2] or sieving devices based on nanoscale gaps [3], electric dc fields of several hundred volts per centimeter are typically used, thus limiting applications in mobile or lab-on-chip devices. Similarly, high pressures are required in deterministic lateral displacement arrays [4,5].

Brownian-motor-based devices were envisioned for particle transport and separation [6] as early as the 1990s. In contrast to the methods mentioned above, Brownian motors transport particles with an ac modulation of either an asymmetric potential [7,8] (flashing ratchets) or a driving force combined with a static ratchet potential [9–12] (rocking ratchets). For flashing ratchets, separation is based on the size dependence of the diffusion coefficient, which is inversely proportional to particle radius [8,11]. Rocking ratchets exhibit a highly nonlinear particle current as a function [10] of the applied force and frequency, which is suggested to be useful for particle separation [10,12]. Recently, we implemented a rocking Brownian motor for nanoparticles [13,14]. We demonstrated the separation of gold spheres measuring 60 and 100 nm in diameter within

a few seconds. The device footprint was small, i.e., less than 20 μm , enabling high fields with voltages of less than 5 V and stable operation over hours. The separation mechanism was based on two intercalated Brownian motors pointing in opposite directions. Particles of different size preferably occupied one of the two motors and were therefore extracted to opposite ends of the device. Modeling suggested that the same separation device was capable of separating two gold sphere populations with a difference in radius of approximately 1 nm [13].

Here, we present a separation device based on a rocking ratchet that splits a particle population into several subpopulations with similar resolution. The device separates the particles by transporting them across increasing potential barriers in the ratchet direction. The separation mechanism is thus markedly different from that of our previous implementation. It exploits the “Arrhenius-like” onset of the particle current with decreasing ratchet potential barriers, which was simulated by Bartussek *et al.* and suggested as a separation mechanism for particles with similar diffusion coefficients [10,12].

In the following, we first describe the experiment and observe the particle current in the device for gold particles nominally 60 nm in diameter. The results agree well with a numerical solution of the Fokker-Planck equation using measured physical parameters as input. Simulations allow us to assess the resolution of the sorting device and its scaling with separation time and force. For the experimental parameters used, we obtain a resolution of 2 nm, which we compare with the experimental resolution based on microscopic inspection after particle deposition.

*ark@zurich.ibm.com

[†]These authors contributed equally to this work.

II. EXPERIMENTAL IMPLEMENTATION

The potential landscape experienced by the particles in our nanofluidic device is based on the electrostatic interaction of charged particles with like-charged walls [15]; see Fig. 1(a). The schematically depicted ratchet with increasing tooth height leads to the aforementioned increase in energy barriers. We note that a similar geometry was used recently for nanofluidic size exclusion [16]. We use 60-nm gold spheres (EM.GC60 from BBI solutions, batch no. 19080123) to study the particle transport in the device. A volume of approximately 30 μl of the suspension is deposited on the sample and subsequently confined to a tunable nanofluidic slit using the nanofluidic confinement apparatus; see SM1 and SM2 of the Supplemental Material [17] and Refs. [13,18] for details. The top boundary of the slit consists of a cover glass with a central mesa of height 40 μm . The lower boundary is a silicon chip [17] with thermal oxide thickness of 235 nm [see Fig. 1(a)]. The geometry of the device is patterned by thermal scanning-probe lithography (*t*-SPL) [19,20] into polyphthalaldehyde (PPA) [see Fig. 1(b)], and then dry-etched into the SiO_2 layer [21]. In the final device, the average height difference

between each of the 19 neighboring teeth is 1.6 nm [see Fig. 1(c)]. Finally, the sample is coated with a 10-nm-thick organic transfer layer (OTL; PiBond Oy) of a polymeric material required to immobilize the particles on the sample surface after sorting [22]. A more detailed description of the sample preparation can be found in SM3 of the Supplemental Material [17]. For imaging, we use interferometric scattering detection (iSCAT) [23,24], recording at 250 frames per second. A temporal stability of the nanofluidic gap of 2 nm rms (see SM4 of the Supplemental Material [17]) is measured using this detection scheme, limited by the stability of our laser source.

The interaction potential $W(x, y, z)$ of charged nanoparticles of radius r in a gap of height h and pattern depth $d(x, y)$ can be approximated by the sphere-plane interaction [13,24,25]

$$W_0 r \psi_S (\psi_{P,1} e^{-\kappa(z-r)} + \psi_{P,2} e^{-\kappa[h+d(x,y)-z-r]}), \quad (1)$$

where $W_0 = 4\pi\epsilon\epsilon_0$, ϵ and ϵ_0 are the relative and the vacuum permittivities, ψ_S , $\psi_{P,1}$, and $\psi_{P,2}$ are the effective surface potentials of the sphere and the two planes,

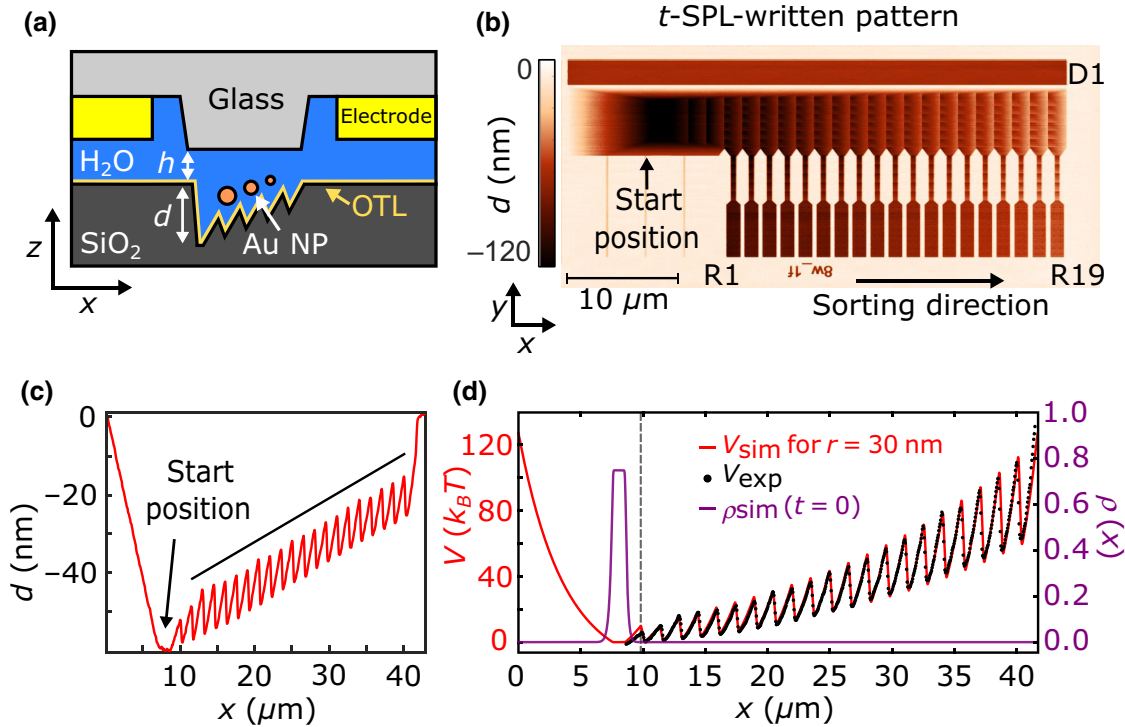


FIG. 1. (a) Schematic side view of the nanofluidic slit (not to scale). A central pillar of 40 μm in height is etched from a cover slip and surrounded by four Cr–Au electrodes. The ratchet structure in SiO_2 is covered with a thin layer of OTL polymer. (b) Topography of the sorting device in PPA after *t*-SPL patterning. From the inclined ratchet (top), particles can be driven into reservoirs (R1 to R19) by linear ratchets after being sorted. Force and diffusivity are measured in D1. (c) Cross section through the device after transfer to SiO_2 measured by atomic force microscopy. The 19 teeth in the sorting ratchet span a vertical distance of 28 nm, corresponding to $\Delta z = 1.6$ nm per tooth. (d) Extrapolated potential $V_{\text{exp}}(x)$ for a gap distance of 64 ± 2 nm (black dots) and the input potential $V_{\text{sim}}(x)$ for simulating the device (red line). We use an initial probability density $\rho_0(x) \propto \exp[-V(x)/k_B T]$ with $0 < x < 10$ μm (dashed line) for our simulations (violet).

z is the vertical particle position measured from the substrate interface, and κ^{-1} is the Debye length; see Fig. 1(a) and [13]. Note that Eq. (1) only holds in the case of a topography with shallow slopes (i.e., < 1) as in our sample. The two-dimensional occupation probability $P(x, y)$ is obtained by integrating the three-dimensional probability density $P(x, y, z) \propto e^{-W(x, y, z)/(k_B T)}$:

$$P(x, y) = \left(C \int_{z=r}^{z=d(x, y)+h-r} e^{-W(x, y, z)/(k_B T)} dz \right), \quad (2)$$

where $k_B T$ is the thermal energy and C is a normalization constant. The free energy $V(x, y)$ up to a reference potential V_0 including positional entropy is given by

$$V(x, y) = -\ln[P(x, y)] + V_0. \quad (3)$$

In order to quantify $V_{\text{exp}}(x)$ experimentally along the ratchet direction x , we trap approximately 30 particles in the ratchet area during the approach of the glass pillar. Their x coordinates are tracked for three gap distances of $h = 151 \pm 2$ nm, $h = 112 \pm 2$ nm, and $h = 103 \pm 2$ nm using Trackpy for Python [17,26,27]. Identifying the normalized frequency of particles observed at position x with the particle occupancy probability $P_{\text{exp}}(x)$ and assuming $\psi_{P,1} = \psi_{P,2} = \psi_P$, we infer from a global fit a Debye length of $\kappa^{-1} = 10.8 \pm 0.1$ nm and $W_0 \psi_S \psi_P = 5.3 \pm 0.2 k_B T/\text{nm}$. Using Eq. (3), we then extrapolate $V_{\text{exp}}(x)$ to other gap distances (see also SM5 of the Supplemental Material [17]).

Size separation experiments are performed at a gap distance of $h = 64 \pm 2$ nm, for which $V_{\text{exp}}(x)$ is shown in Fig. 1(d). The particles are first transported to the starting position of the ratchet [see Fig. 1(c)], which corresponds to the lowest energy in the system. In order to speed up the process we exploit the previously observed reversal of the particle current in rocking Brownian motors [14] at rocking frequencies above 150 Hz. Using 2 to 3 V and a frequency of 300 to 500 Hz across each pair of electrodes, the particles are transported to the starting position within a few minutes.

Next, we apply an ac voltage of 3.5-V amplitude at a frequency of 5 Hz to drive the particles in the x direction (see Fig. 1). A second voltage of 3-V amplitude at 500 Hz generates a field along the y axis and prevents particles from diffusing into the reservoirs, again exploiting current reversal [14]. Three representative frames of the transport process are shown in Fig. 2(a) together with the measured particle occupancy for each tooth in the ratchet. For particles entering the ratchet, the observed particle speed is of the order of tens of $\mu\text{m}/\text{s}$, and slows down dramatically after 5 s. From 10 to 20 s, the population shifts on average by just one tooth. In this state, the particle population is spread over 13 teeth, indicating a fine separation of particles.

III. MODELING

The dynamics of a Brownian motor with ratchet potential $V(x)$ and an external rocking force $F(t)$ can be expressed in terms of a probability density $\rho(x, t)$, which obeys the Fokker-Planck equation [28]:

$$\partial_t \rho(x, t) = \partial_x \left[\left(\frac{1}{\gamma} \partial_x \tilde{V}(x, t) + D_0 \partial_x \right) \rho(x, t) \right], \quad (4)$$

where γ is the drag constant, D_0 is the diffusion coefficient, and $\tilde{V}(x, t) = V(x) + xF(t)$ is the tilted potential. The sorting process represents an initial-value problem where $\rho_0(x)$ of the unsorted particles at $t = 0$ is transformed into $\rho_{\text{final}}(x)$ of the sorted particles. The propagation of $\rho_0(x) \rightarrow \rho_{\text{final}}(x)$ is given by Eq. (4) and can normally be calculated only numerically. Therefore, we discretize Eq. (4) with respect to x and approximate the spatial derivatives by finite differences. The resulting system of ordinary differential equations is then computed by standard solvers for ordinary differential equations. For more details of the numerical solution of Eq. (4), see SM6 of the Supplemental Material [17]. We use the extrapolated interaction potential as input [see Fig. 1(d)] and a rocking force F that is inferred [13] from the average drift speed $\langle v_{\text{drift}} \rangle$ of the particles in the 30-nm-deep drift field D1 [see Fig. 1(b)] of $F = k_B T \langle v_{\text{drift}} \rangle / D_0 = 20.7 \pm 1.3 k_B T / \mu\text{m}$. The average diffusion constant $D_0 = 3.2 \pm 0.2 \mu\text{m}^2/\text{s}$ is determined for particles in field D1 without applied fields.

According to the manufacturer, the mean radius of the gold nanoparticles is 30.3 nm, and their coefficient of variation is 8%. Assuming a Gaussian size distribution, this results in 97.5% of the particles having a radius of between 25 and 35 nm. We simulate particle sizes in this range with a radial difference of 1 nm, and scale $V(x)$ [Eq. (1)], $F \propto r$ and $D_0 \propto r^{-1}$, accordingly [13]. Each particle species is simulated separately. The resulting probability densities are then summed up and weighted with their corresponding relative portion in the original dispersion (see also SM7 of the Supplemental Material [17]). The resulting particle probability distribution $P_{\text{sim}}(x)$ after 1, 10, and 20 s of sorting can be seen in Fig. 2(a). This agrees well with the experimentally observed evolution of $P_{\text{exp}}(n)$.

The temporal evolution of the mean travel distance $\langle x_r \rangle$ for particles with different radii r is shown in Fig. 2(b) and reflects the observation of Bartussek *et al.* [10] of an Arrhenius-like decrease of the particle current with increasing energy barriers. After a fast transport into the ratchet, the average speed decreases sharply, and the particles enter a quasisteady state. For particles of different sizes, the transition occurs at a different tooth number because smaller particles experience less interaction potential for the same tooth height [see Eq. (1)]. As a result, particles of different sizes are transported to different locations in the device [see Fig. 2(c)].

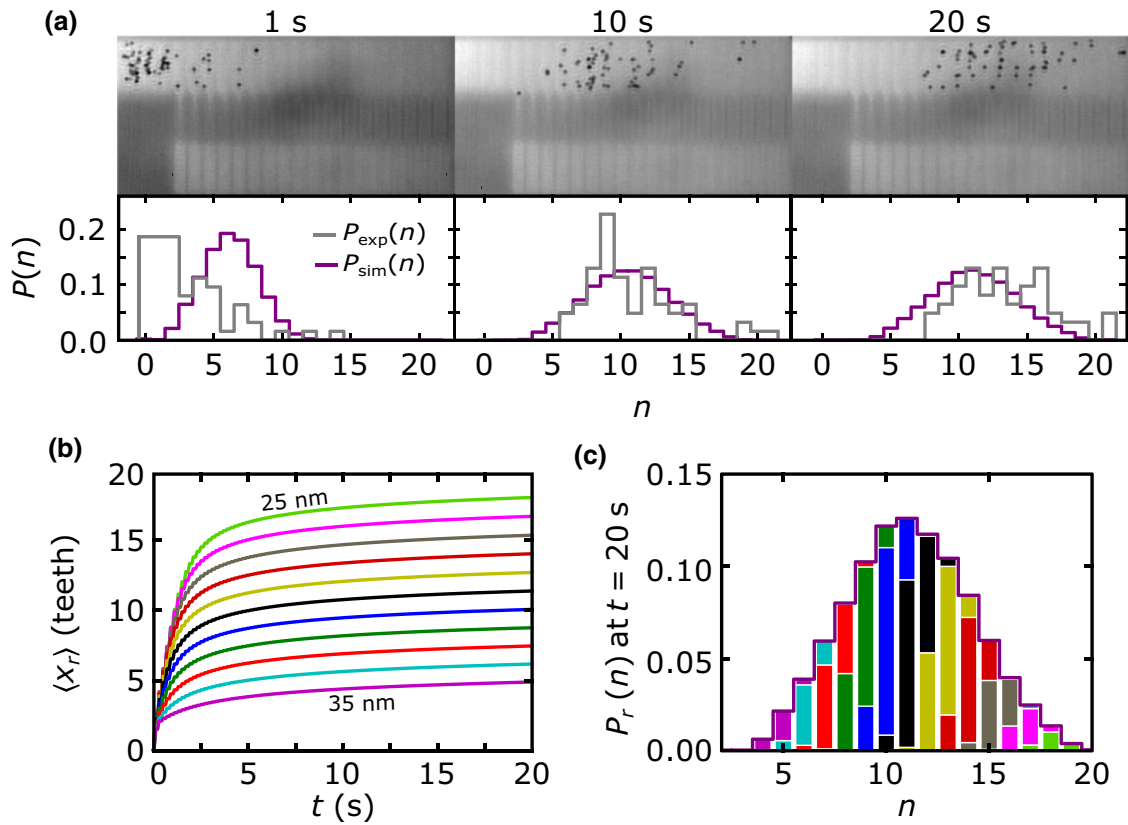


FIG. 2. (a) Top: iSCAT images of the sorting process after 1, 10, and 20 s of an applied ac voltage of 3.5 V at 5 Hz. Bottom: comparison of the experimental, $P_{\text{exp}}(n)$, and simulated, $P_{\text{sim}}(n)$, particle distributions. (b) Expected average travel distance for particles of radii between 25 and 35 nm with 1 nm difference in radius as a function of time. (c) Simulated probability distribution $P_r(n)$ after 20 s of sorting. The width of the distributions of single particle types, marked by separate colors, indicates the simulated resolution of the sorting device. The color code corresponds to that used in (b).

The behavior of the particle transport into the device is almost entirely controlled by the energy landscape experienced by the particles in the forward bias case. The backward current is significant only in the first 2.5 s of the experiment, and then becomes negligible for all considered particle sizes (see SM8 of the Supplemental Material [17]). The forward energy barriers are plotted in Fig. 3(a). Depending on the particle size, the barriers start to deviate from zero at different tooth numbers. After sorting durations of 5 to 20 s, the particles on average arrive at energy barriers between 3 and $6 k_B T$.

The rapidly increasing energy barriers lead to a focusing of the particle density. This can be seen from the standard deviation σ_t of the particle distribution across the ratchet teeth measured for each particle population as shown in Fig. 3(b). σ_t increases within the first few seconds and then decreases to less than one tooth after $t \approx 5$ s. σ_t is related to the spread σ_r of particle radii in a given tooth [different colors per tooth in Fig. 2(c)], and we find $\sigma_r/\text{nm} = 0.76\sigma_t$ shown as the right-hand y axis in Fig. 3(b) (for details see SM9 of the Supplemental Material [17]). σ_r rapidly approaches a value of less than 0.6 nm after 5 s, and then

decreases slowly to approximately 0.5 nm after 20 s. If we define the resolution [29] of the device to be $4\sigma_r$, it follows that we can separate two particles with a difference in radius of 2 nm.

As σ_r depends exclusively on the forward-biased energy landscape, the only tunable parameter to increase the resolution in a device, for a given time span, is the amplitude of the force. A higher force leads to more steeply increasing energy barriers as a consequence of their exponential scaling with x [see Fig. 3(c)]. As a result, the separation resolution increases. This can be seen from the decrease of σ_r shown in Fig. 3(d). For this device, the sorting resolution scales roughly as a power law of $F^{-0.39}$ and reaches $\sigma_r \approx 0.4$ nm at $30k_B T/\mu\text{m}$.

IV. EXPERIMENTAL RESOLUTION FOR SEPARATING SPHERES

After the sorting process, the particles are transported to compartments R1 to R19 [Fig. 1(b)] and deposited onto the surface for further inspection (see SM10 of the Supplemental Material for details [17]). However, because of

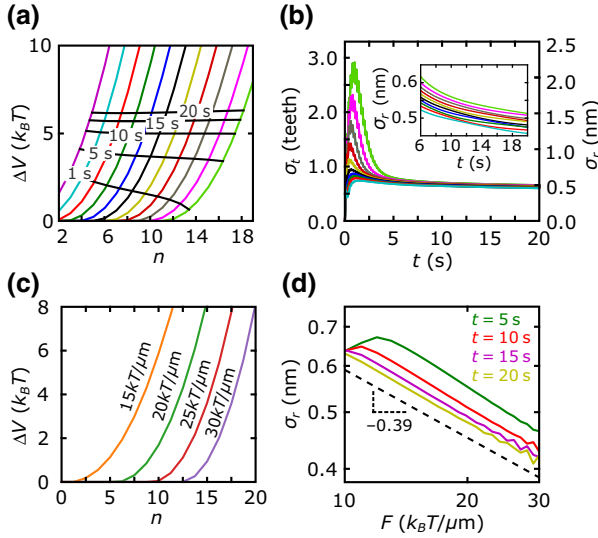


FIG. 3. (a) Forward bias potential barriers for particles with radius 35 to 25 nm (left to right) and a force of $20.7 k_B T/\mu\text{m}$ (colored lines). The intercept with the black lines marks the average travel distances and barrier heights reached after 5, 10, 15, and 20 s. (b) Standard deviation σ_r of the radius distribution in the central tooth for each particle size. The inset shows an enlarged view for longer sorting durations. (c) Remaining energy barriers under forward bias for particles with a radius of 30 nm and applied forces of 15, 20, 25, and $30 k_B T/\mu\text{m}$. (d) σ_r as a function of applied force and different separation durations.

the thin polymer film, we observe plastic deformation during the immobilization process. Therefore, we perform a second experiment using a mixture of gold spheres with radii of 80 and 100 nm (EM.GC80 and EM.GC100 from BBI solutions, batch nos. 13063 and 13083) and a thick polymer layer. Specifically, the polymer stack consists of 52 nm of the adhesion promoter HM8006 (JSR Inc.) and 185 nm of PPA. The thick polymer layer renders plastic deformation unlikely, as shown recently [22].

After sorting, we quantify the particle size using scanning electron microscopy (SEM) and atomic force microscopy (AFM). Similar to what has been observed previously [13], the particles show a variety of shapes. As well as spheres, we find flat plates and particles with clearly exposed crystal planes, which we label diamonds [see Figs. 4(a) and 4(b)].

Figure 4(c) shows the measured effective radius of the particles given by $r^2\pi = A$, where A is determined from SEM images using thresholding (see SM11 of the Supplemental Material [17] for details). We note that we treat all systematic errors in SEM imaging by fitting the offset of the line resulting from the model to measured radii of spherical particles. This treatment does not affect our discussion on separation resolution. The spherical particles are well separated with high resolution and follow the predictions of the model (dashed line and shaded area);

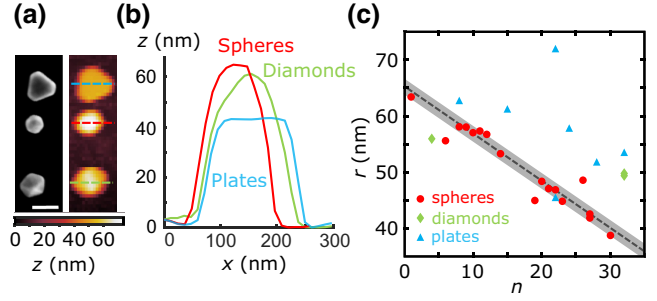


FIG. 4. (a) SEM (left) and AFM (right) scans of the different particle types present in a mixture with nominal radii of 40 and 50 nm. The white scale bar indicates 100 nm. (b) AFM scan across particles from (a). (c) Quantification of the sorting, with colors corresponding to the particle types shown in (b). The spherical particles (red) follow a linear trend of particle radius r and tooth number n . The slope of the dashed line is obtained from simulation and its position is shifted in r to obtain a good fit to the data. The shaded area corresponds to a width of $\pm 2\sigma_r$. The plates (blue) and diamonds (green) show a different behavior because they experience a reduced interaction energy compared with spherical particles.

see SM12 of the Supplemental Material [17] for details. Counting all spheres, we measure a standard deviation of 2 nm with respect to the model. We note that in our experiments the measured gap distance is stable in time to only 2 nm rms, partially due to laser noise. This fact will induce hard-to-predict variations in the travel distance of similar particles. Given these uncertainties, the experimental data corroborate the simulation results. The plates and diamonds, however, have a flatter shape, and therefore cannot be described by the spherical particle model. The smaller ratio between particle height and diameter reduces their interaction energy with the device surfaces, according to Eq. (1). Consequently, a plate or diamond of the same area as a sphere is transported further into the ratchet.

V. CONCLUSION

We characterize a nanoparticle sorting device based on a nanofluidic rocking Brownian motor with a linearly increasing tooth height. Simulations predict a separation resolution of approximately 2 nm (4σ) in radius, which is consistent with the experimentally measured resolution for spherical particles of 2 nm (1σ) given the experimental conditions. However, particles of different shapes are also transported according to their smallest diameter and therefore cannot be fully separated from the spheres in such a one-dimensional device. Combined with a separation mechanism that differentiates by hydrodynamic radius, a two-dimensional sorting could be implemented that would allow separation by size and smallest particle diameter. Equation (1) suggests that particles of the same size and different surface potential can also be separated, but with

lower resolution because the charge affects only the prefactor and not the exponent. Our modeling shows that, for the 60-nm particles, a 10% change in surface potential is required to have the same effect as a 1-nm difference in radius. The method is accordingly separating mainly by size rather than charge.

Similar to conventional devices, the separation resolution is enhanced with increasing external driving force. However, for our devices, not the absolute force but rather the energy per ratchet tooth is important. Thus, higher resolution can be obtained by simply stretching the geometry of the ratchet, and resolutions below 1 nm would be within reach.

The fast sorting of the particles, achieved in 5–10 s, is promoted by the small footprint of the device. Therefore, rocking Brownian motors combine high-resolution separation with low applied voltages, high speed, and small device footprints, rendering them ideal for future lab-on-chip applications.

ACKNOWLEDGMENTS

We thank U. Drechsler for assistance in fabricating the glass pillars, H. Wolf for stimulating discussions, and R. Allenspach and H. Riel for support. Funding is provided by the European Research Council (StG No. 307079, PoC Grant No. 825794) and the Swiss National Science Foundation (SNSF No. 200021-179148).

-
- [1] T. Salafi, K. K. Zeming, and Y. Zhang, Advancements in microfluidics for nanoparticle separation, *Lab Chip* **17**, 11 (2017).
- [2] H. Swerdlow and R. Gesteland, Capillary gel electrophoresis for rapid, high resolution DNA sequencing, *Nucleic Acids Res.* **18**, 1415 (1990).
- [3] J. Fu, R. B. Schoch, A. L. Stevens, S. R. Tannenbaum, and J. Han, A patterned anisotropic nanofluidic sieving structure for continuous-flow separation of DNA and proteins, *Nat. Nanotechnol.* **2**, 121 (2007).
- [4] L. R. Huang, E. C. Cox, R. H. Austin, and J. C. Sturm, Continuous particle separation through deterministic lateral displacement, *Science* **304**, 987 (2004).
- [5] B. H. Wunsch, J. T. Smith, S. M. Gifford, C. Wang, M. Brink, R. L. Bruce, R. H. Austin, G. Stolovitzky, and Y. Astier, Nanoscale lateral displacement arrays for the separation of exosomes and colloids down to 20 nm, *Nat. Nanotechnol.* **11**, 936 (2016).
- [6] P. Hänggi and F. Marchesoni, Artificial Brownian motors: Controlling transport on the nanoscale, *Rev. Mod. Phys.* **81**, 387 (2009).
- [7] J. Rousselet, L. Salome, A. Ajdari, and J. Prost, Directional motion of brownian particles induced by a periodic asymmetric potential, *Nature (London)* **370**, 446 (1994).
- [8] L. Gorre-Talini, S. Jeanjean, and P. Silberzan, Sorting of Brownian particles by the pulsed application of an asymmetric potential, *Phys. Rev. E* **56**, 2025 (1997).1063-651X
- [9] M. O. Magnasco, Forced Thermal Ratchets, *Phys. Rev. Lett.* **71**, 1477 (1993).
- [10] R. Bartussek, P. Hänggi, and J. G. Kissner, Periodically rocked thermal ratchets, *Europhys. Lett.* **28**, 459 (1994).
- [11] L. P. Faucheux and A. Libchaber, Selection of Brownian particles, *J. Chem. Soc., Faraday Trans.* **91**, 3163 (1995).
- [12] P. Reimann and P. Hänggi, Introduction to the physics of Brownian motors, *Appl. Phys. A* **75**, 169 (2002).
- [13] M. J. Skaug, C. Schwemmer, S. Fringes, C. D. Rawlings, and A. W. Knoll, Nanofluidic rocking Brownian motors, *Science* **359**, 1505 (2018).
- [14] C. Schwemmer, S. Fringes, U. Duerig, Y. K. Ryu, and A. W. Knoll, Experimental Observation of Current Reversal in a Rocking Brownian Motor, *Phys. Rev. Lett.* **121**, 104102 (2018).
- [15] M. Krishnan, N. Mojarad, P. Kukura, and V. Sandoghdar, Geometry-induced electrostatic trapping of nanometric objects in a fluid, *Nature (London)* **467**, 692 (2010).
- [16] K. T. Liao, J. Schumacher, H. J. Lezec, and S. M. Stavis, Subnanometer structure and function from ion beams through complex fluidics to fluorescent particles, *Lab Chip* **18**, 139 (2018).
- [17] See Supplemental Material at <http://link.aps.org/supplemental/10.1103/PhysRevApplied.15.034006> for additional information.
- [18] S. Fringes, F. Holzner, and A. W. Knoll, The nanofluidic confinement apparatus: Studying confinement-dependent nanoparticle behavior and diffusion, *Beilstein J. Nanotechnol.* **9**, 301 (2018).
- [19] D. Pires, J. L. Hedrick, A. De Silva, J. Frommer, B. Gotsmann, H. Wolf, M. Despont, U. Duerig, and A. W. Knoll, Nanoscale three-dimensional patterning of molecular resists by scanning probes, *Science* **328**, 732 (2010).
- [20] R. Garcia, A. W. Knoll, and E. Riedo, Advanced scanning probe lithography, *Nat. Nanotechnol.* **9**, 577 (2014).
- [21] C. D. Rawlings, M. Zientek, M. Spieser, D. Urbonas, T. Stöferle, R. F. Mahrt, Y. Lisunova, J. Brugger, U. Duerig, and A. W. Knoll, Control of the interaction strength of photonic molecules by nanometer precise 3D fabrication, *Sci. Rep.* **7**, 16502 (2017).
- [22] S. Fringes, C. Schwemmer, C. D. Rawlings, and A. W. Knoll, Deterministic deposition of nanoparticles with sub-10 nm resolution, *Nano Lett.* **19**, 8855 (2019).
- [23] K. Lindfors, T. Kalkbrenner, P. Stoller, and V. Sandoghdar, Detection and Spectroscopy of Gold Nanoparticles Using Supercontinuum White Light Confocal Microscopy, *Phys. Rev. Lett.* **93**, 037401 (2004).
- [24] S. Fringes, M. J. Skaug, and A. W. Knoll, In situ contrast calibration to determine the height of individual diffusing nanoparticles in a tunable confinement, *J. Appl. Phys.* **119**, 024303 (2016).
- [25] S. H. Behrens and D. G. Grier, The charge of glass and silica surfaces, *J. Chem. Phys.* **115**, 6716 (2001).

- [26] D. Allan, T. Caswell, N. Keim, and C. van der Wel, Trackpy version 0.3.2 for Python, download available at <http://doi.org/10.5281/zenodo.60550> (2016).
- [27] J. C. Crocker and D. G. Grier, Methods of digital video microscopy for colloidal studies, *J. Colloid Interface Sci.* **179**, 298 (1996).
- [28] H. Risken, *The Fokker-Planck Equation* (Springer, Berlin, 1989), 2nd ed.
- [29] I. Derényi and R. Dean Astumian, AC separation of particles by biased Brownian motion in a two-dimensional sieve, *Phys. Rev. E* **58**, 7781 (1998).1063-651X